

A MINI-BAL OUTFLOW AT 900 PC FROM THE CENTRAL SOURCE: VLT/X-SHOOTER OBSERVATIONS

XINFENG XU^{1,†}, NAHUM ARAV¹, TIMOTHY MILLER¹, CHRIS BENN²

¹Department of Physics, Virginia Tech, Blacksburg, VA 24061, USA and

²Isaac Newton Group, Apartado 321, 38700 Santa Cruz de La Palma, Spain

Draft version May 7, 2018

ABSTRACT

We determine the physical conditions and location of the outflow material seen in the mini-BAL quasar SDSS J1111+1437 ($z = 2.138$). These results are based on the analysis of a high S/N, medium-resolution VLT/X-shooter spectrum. The main outflow component spans the velocity range -1500 to -3000 km s⁻¹ and has detected absorption troughs from both high-ionization species: C IV, N V, O VI, Si IV, P V, and S IV; and low-ionization species: H I, C II, Mg II, Al II, Al III, Si II, and Si III. Measurements of these troughs allow us to derive an accurate photoionization solution for this absorption component: a hydrogen column density, $\log(N_{\text{H}}) = 21.47_{-0.27}^{+0.21}$ cm⁻² and ionization parameter, $\log(U_{\text{H}}) = -1.23_{-0.25}^{+0.20}$. Troughs produced from the ground and excited states of S IV combined with the derived U_{H} value allow us to determine an electron number density of $\log(n_{\text{e}}) = 3.62_{-0.11}^{+0.09}$ cm⁻³; and to obtain the distance of the ionized gas from the central source: $R = 880_{-260}^{+210}$ pc.

Keywords: galaxies: active – galaxies: kinematics and dynamics – quasars: absorption lines – ISM: jets and outflows

1. INTRODUCTION

Quasar outflows are often detected as blueshifted absorption troughs in the rest-frame of the active galactic nucleus (AGN) spectrum (Hewett & Foltz 2003; Dai et al. 2008; Knigge et al. 2008; Ganguly & Brotherton 2008). These outflows are often invoked as agents for active galactic nuclei (AGN) feedback (e.g., Ostriker et al. 2010; Ciotti et al. 2010; McCarthy et al. 2010; Hopkins & Elvis 2010; Soker & Meiron 2011; Faucher-Giguère et al. 2012; Choi et al. 2014; Hopkins et al. 2016; Anglés-Alcázar et al. 2017; Ciotti et al. 2017). A crucial parameter needed to assess the contribution of the outflow to AGN feedback is the distance (R) of the outflow from the central source, which can be inferred from excited-state absorption combined with photoionization modeling (e.g., Korista et al. 2008). Using this method over the last decade, our group and other collaborations measured R for about 20 AGN outflows (Hamann et al. 2001; de Kool et al. 2001, 2002a,b; Gabel et al. 2005; Moe et al. 2009; Bautista et al. 2010; Dunn et al. 2010; Aoki et al. 2011; Arav et al. 2012; Borguet et al. 2012a,b, 2013; Edmonds et al. 2011; Arav et al. 2013; Lucy et al. 2014; Finn et al. 2014; Chamberlain & Arav 2015; Chamberlain et al. 2015). These investigations located the outflows at an R range of several parsecs to many kilo-parsecs. For luminous quasars, the majority of these findings were at R of hundreds to thousands of parsecs scales (see Arav et al. 2013 for details). Most of the R determinations referenced above arise from singly ionized species (mainly Fe II and Si II). However, the majority of outflows show absorption troughs only from more highly ionized species. Hence, the applicability of R derived from singly ionized species to the majority of outflows is

somewhat model-dependent (see discussion in § 1 of Dunn et al. 2012). To address this issue empirically, R determinations using doubly and triply ionized species are needed.

Using ground-based telescopes, the main high-ionization species with a measurable trough arising from an excited state is S IV. This ion has resonance and excited level transitions at 1062.66Å/1072.97Å, respectively. To measure absorption troughs from these transitions, we conducted a survey using the VLT/X-shooter spectrograph between 2012 and 2014. From this survey we published four R determinations using S IV troughs (Borguet et al. 2013; Chamberlain et al. 2015). Here, we present another such determination for the object SDSS J1111+1437.

The layout of this paper is as follows. In Section 2, we present the VLT/X-shooter observation of SDSS J1111+1437. In Section 3, we analyze the spectrum and extract column densities from the absorption troughs. In Section 4, we describe the photoionization analysis that determines the ionization parameter and total hydrogen column density of the outflow. In Section 5, we analyze the density-sensitive troughs from S IV and S IV* to determine the electron number density n_{e} of the outflow. In Section 6, we present our distance and energetics results. Finally, we summarize our method and findings in Section 7.

2. OBSERVATION AND DATA REDUCTION

SDSS J1111+1437 (J2000: R.A. = 11:11:10.15, decl. = +14:37:57.1, $z = 2.138$) was observed with the VLT/X-shooter in January 2014 as part of our program 092.B-0267 (PI: Benn). X-shooter is the second-generation, medium spectral resolution ($R \sim 6000 - 9000$) spectrograph installed on the VLT. It covers a wide spectral band (3000 – 24,000Å) in a single exposure by its unique design, where the incoming light is split into three independent arms (UVB, VIS and NIR). The wide spectral

[†] Email: xinfeng@vt.edu

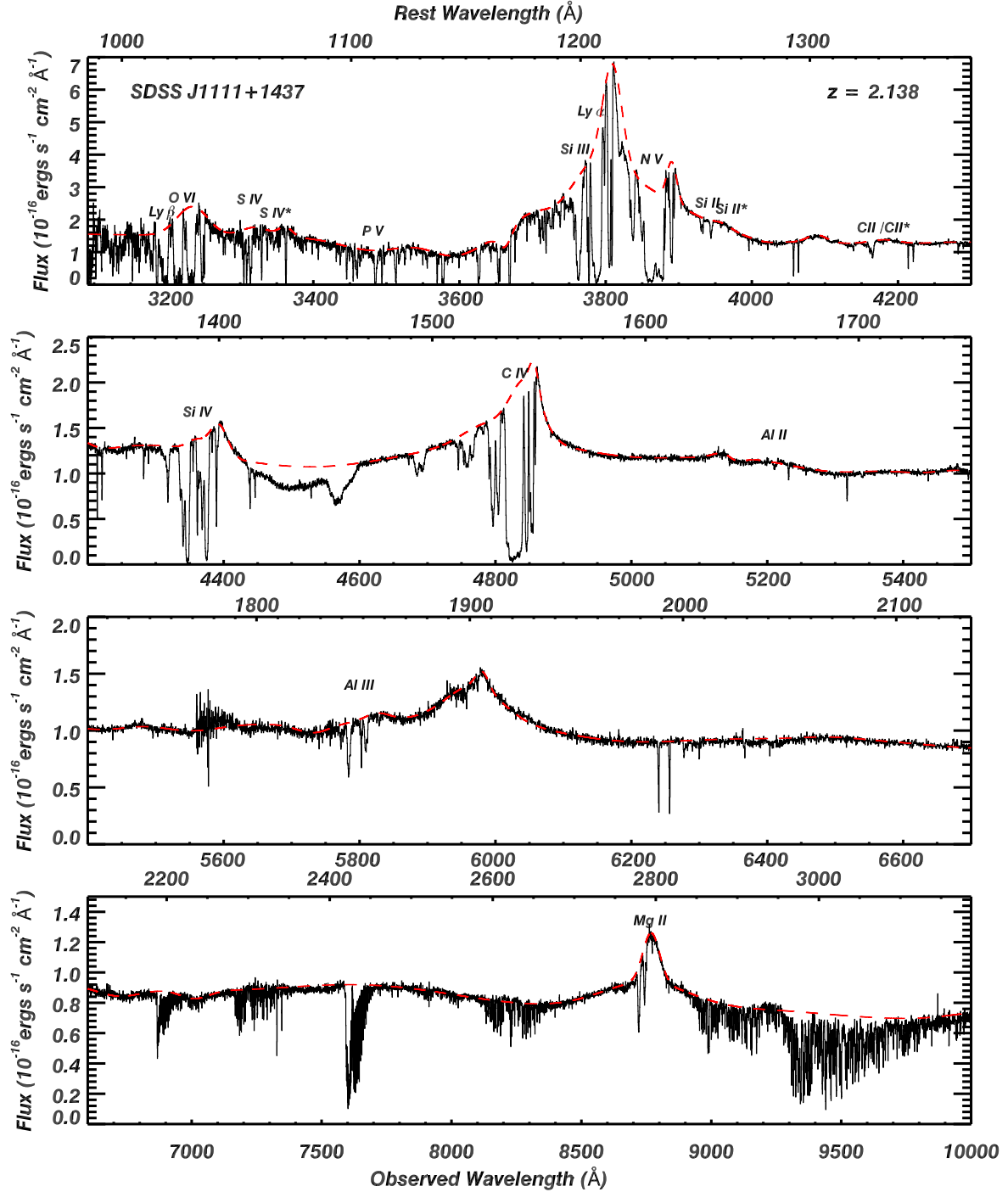


Figure 1. VLT/X-shooter spectrum of the quasar SDSS J1111+1437 ($z = 2.138$). We label the ionic absorption troughs associated with the outflow and represent the unabsorbed emission model with a red dashed line (see Section 2). Narrow absorption from intervening systems appear throughout the spectrum, and terrestrial absorption from molecular O_2 in our atmosphere is seen near 6850 \AA and 7600 \AA (observed frame), but none of these features affect the analysis presented in this paper. We note the high-velocity C IV mini-BALs around 1530 \AA , 1515 \AA , 1495 \AA as well as the even higher velocity C IV BAL around 1420 \AA – 1460 \AA . However, due to the lack of diagnostic troughs, we do not analyze these four outflows in this paper. The troughs from these high-velocity systems do not affect the analysis results of the outflow component we concentrate on in this paper.

Table 1
Measured Column Densities

Ion (1)	AOD ^a (2)	PC (3)	PL (4)	Adopted (5)
H I	>9800			> 9800–1960
C II	>320			> 320–64
C IV	>3100			> 3100–620
N V	>5100			> 5100–1020
O VI	>6600			> 6600–1320
Mg II	> 44	53.6 ^{+0.4} _{-0.4}	58 ^{+2.8} _{-1.7}	53.6 ^{+7.2} _{-10.1}
Al II	> 2.8			> 2.8–0.56
Al III	> 48	56.6 ^{+1.6} ₋₂	68 ^{+8.6} _{-5.2}	56.6 ⁺²⁰ _{-8.6}
Si II	> 30			> 30–8.5
Si III	> 200			> 200–40
Si IV	> 700			> 700–140
P V	> 144	145 ⁺¹⁶ ₋₁₆	155 ⁺¹⁸ ₋₂₀	145 ⁺²⁸ ₋₁₆
S IV	> 3400 ⁺⁴⁵⁰ ₋₄₅₀			> 3400 ⁺⁴⁵⁰ ₋₄₅₀
S IV*	> 800 ⁺¹²⁵ ₋₁₂₅			> 800 ⁺¹²⁵ ₋₁₂₅

Note. —

^a The velocity integration range for the AOD method is from -2200 to -1500 km s⁻¹. Columns (2),(3),(4): The integrated column densities for the three absorber models, in units of 10¹²cm⁻². The errors are computed from photon statistics (S/N). Column (5): Adopted values for the photoionization analysis. The computation of the adopted error bars is described in Section 3.2.

coverage allows the detection of absorption troughs from the ionic species H I, C II, C IV, N V, O VI, Mg II, Al II, Al III, Si II, Si III, Si IV, P V and S IV/S IV* (see figure 1). The width (1500 km s⁻¹) of the C IV trough satisfies the definition of a mini-BAL outflow (Hamann & Sabra 2004).

We reduced the SDSS J1111+1437 spectra using the ESO Reflex workflow (Ballester et al. 2011). The one-dimensional spectra extracted were then coadded after manually performing cosmic-ray rejection on each spectrum. We present the reduced UVB+VIS+NIR spectrum of SDSS J1111+1437 in figure 1.

We do not show the observed spectra between 1 ~ 2.5 μ m. As in this spectral range, we found no absorption troughs associated with the outflow system we analyze here. We note that, in particular, no H α and H β absorption troughs were found. Existence of such troughs would suggest a higher number density for the outflow than we derive in section 5 (e.g., see Sun et al. 2017). Therefore, their absence is consistent with the results of our analysis.

3. SPECTRAL FITTING

3.1. Unabsorbed Emission Model

Generally, the UV unabsorbed emission source in AGNs can be modeled by two components: a continuum that is often described by a power law and emission lines that are usually modeled by a set of ad hoc Gaussian profiles. These emission lines can be divided into broad emission lines (BELs) and narrow emission lines.

We fit the continuum with a power law and where the fit is poor (1090 \AA – 1170 \AA and 2100 \AA – 2300 \AA rest-frame), we correct it by a cubic spline. The power law is in the form of $F(\lambda) = F_{1100}(\lambda/1100)^\alpha$, where $F_{1100} = 1.5 \times 10^{-16}$ ergs⁻¹cm⁻² \AA^{-1} is the observed flux at 1100 \AA

(rest-frame) and $\alpha = -0.704$. Figure 1 shows our full unabsorbed emission model fitted to the data.

3.2. Modeling of Blended Troughs and Column Density Measurements

An outflow system is identified by absorption troughs from different lines that cover a similar velocity range. In SDSS J1111+1437, the analyzed outflow spans $-2200 < v < -1500$ km s⁻¹. To derive the ionic column density, the simplest model is the apparent optical depth (AOD) method, where $\tau(\lambda) \equiv -\ln(I(\lambda))$, $I(\lambda) = F_{obs}(\lambda)/F_0(\lambda)$ is the residual intensity and F_{obs} is the observed flux. The optical depth, τ , is then used to calculate the associated column density, N_{ion} (e.g. Equation (9) in Savage & Sembach 1991). However, AOD analysis usually gives a lower limit for column densities due to non-black saturation in the troughs of AGN outflows (e.g., Arav et al. 2008; Borguet et al. 2012a, 2013; Chamberlain et al. 2015; Arav et al. 2018). Therefore, for singlet lines we use the AOD measurement only as a lower limit.

For doublet and multiplet line troughs, we can use the partial-covering (PC) and power-law (PL) absorption models to overcome the non-black saturation problem (Arav et al. 1999; de Kool et al. 2002b; Borguet et al. 2012a; Chamberlain et al. 2015). However, self-blending exists in the C II, C IV and N V troughs, and blending with the Ly α forest affects the S IV, P V and O VI troughs. For these cases, we can only use the template fitting method (Moe et al. 2009; Borguet et al. 2013; Chamberlain et al. 2015; Arav et al. 2018). The main assumption in the template fitting method is that ions with a similar ionization potential will have similar optical depth profiles as a function of velocity. In this case, unblended troughs can be used as a template to fit a Gaussian profile in optical depth. Then the blended troughs can be fitted with this Gaussian profile by scaling the Gaussian’s depth but leaving the shape and centroid velocity unchanged.

We chose the unblended Al III 1854.72 \AA trough as the template for the low-ionization troughs, including C II, Mg II and Si II, while high-ionization troughs, like C IV, N V, O VI and S IV, were fitted by the Si IV 1402.77 \AA template. The main reasons for choosing these two troughs are: 1. the wide velocity separation between their blue and red component of the doublet along with the width of the outflow prevents self-blending; 2. these two troughs are not contaminated by other intervening absorption lines; and 3. the low-ionization species have similar ionization potentials to Al III, while the high-ionization species have ionization potentials closer to that of Si IV. For both of these templates, we keep the centroid velocity and width fixed and change the scaling of the template to get the best fitting for other troughs. Then we extract ionic column densities using the methods described in Chamberlain & Arav (2015), using the AOD, PC, and PL methods on the fitted templates. See figures 2 and 3 for more details on the template and table 1 for each ion’s column density.

The final column density value adopted for each ion follows these rules. If a PC measurement exists, we choose it as the adopted value. The upper error bar is set to

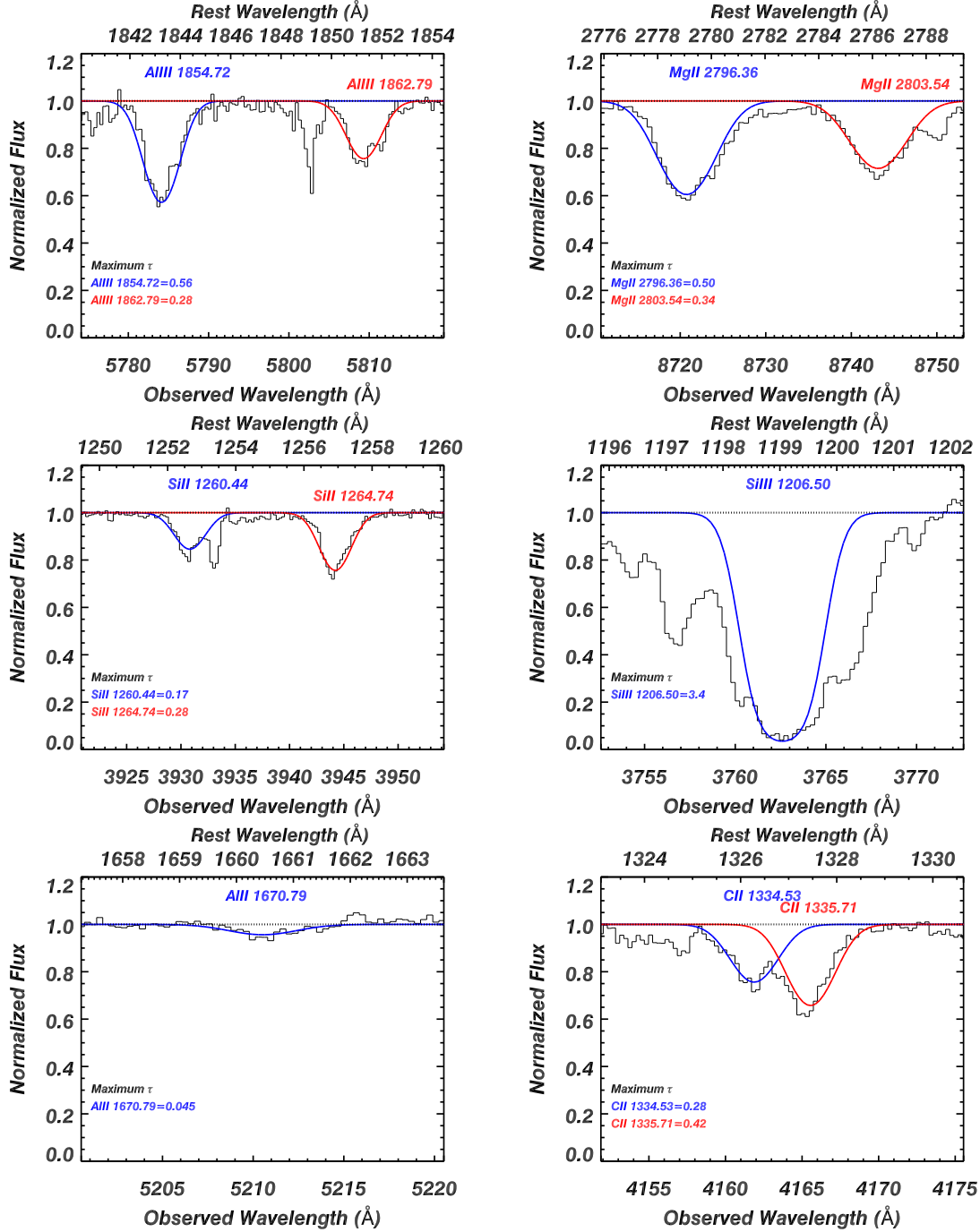


Figure 2. Fits to the low-ionization species' absorption troughs observed in the X-shooter spectrum of SDSS J1111+1437. The Al III blue (1854.72Å) trough is used for the Gaussian template fit. The Gaussian templates for the shorter- and longer-wavelength transitions are shown in blue and red, respectively. Maximum τ shown in the panels is the maximum optical depth of the fitted template.

be the PL's upper bound minus the PC column density value, while the lower error is the PC measurement minus the AOD column density value. In this way, we take into account the systematic error that is due to different absorption models (Chamberlain et al. 2015). If the trough is from a singlet, we choose the AOD measurement as a lower limit. The lower error of the the adopted AOD value is fixed at 20%. This includes the systematic error of the emission model in the template fitting.

Examining figures 2 and 3 demonstrates the advantages of the template fitting approach. First, the tem-

plate fitting to the Al III, Mg II, S III and C II troughs in Figure 2 show good matches to the data, which increase our confidence that these troughs are close to the apparent optical depth case, and therefore do not suffer from much non-black saturation. The minor substructure within these absorption features that are not well matched by smooth Gaussian templates, contributes less than 5% error to the column densities of the above troughs. Second, as mentioned above, the template fits allow us to extract column densities for troughs in the Ly α forest, by ignoring the contaminating troughs.

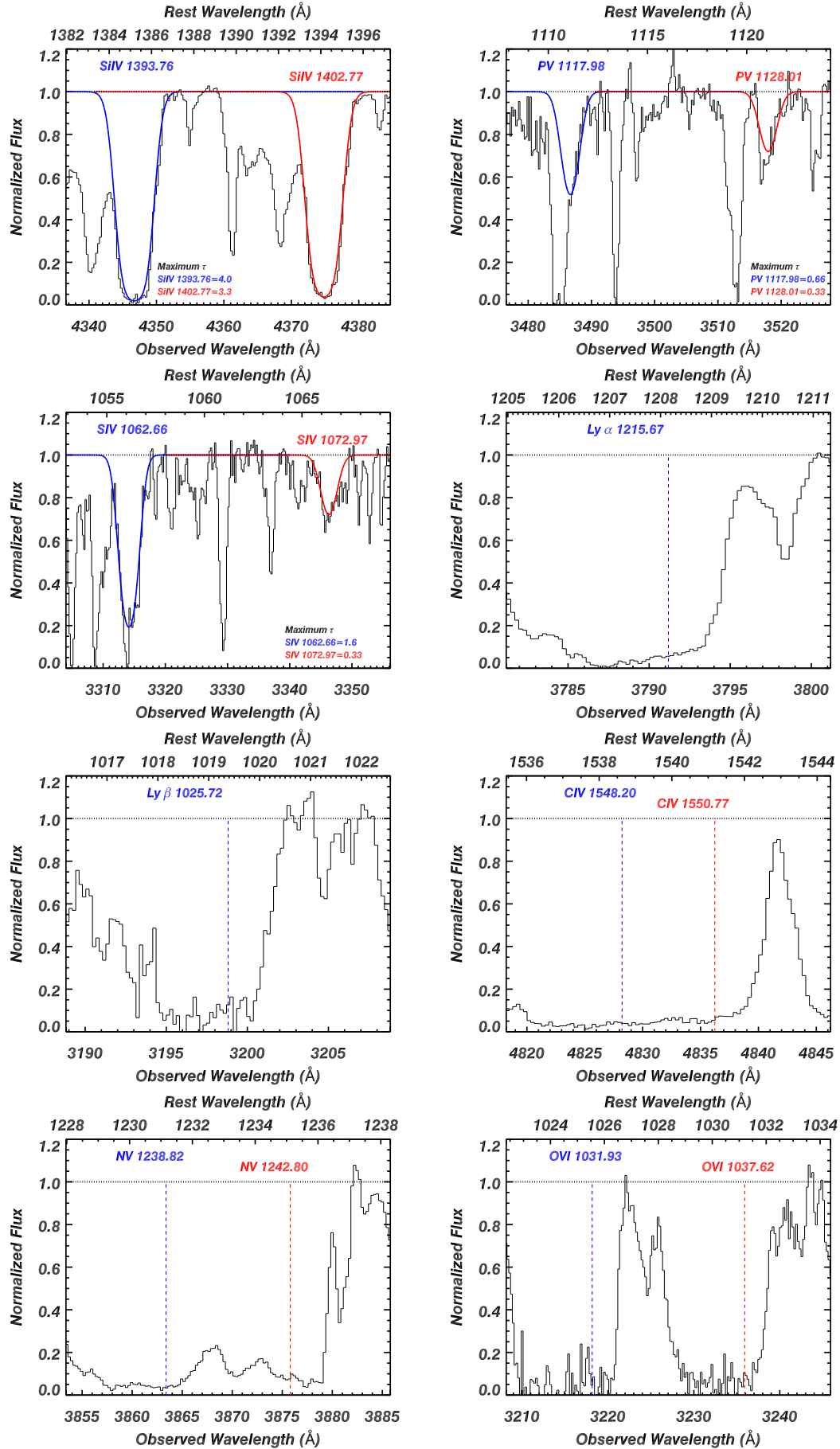


Figure 3. Same as figure 2 but for the high-ionization species and the saturated Ly α and Ly β troughs. The SiIV red (1402.77Å) trough is used for the Gaussian template fit. For the saturated line troughs where template fitting is not adopted, the column density integration range is $-2200 < v < -1500 \text{ km s}^{-1}$.

This attribute is crucial for the diagnostic P V and S IV troughs.

3.3. The Low-Ionization Troughs

The Al III doublet troughs are well separated without any contamination, and the optical depth ratio between the Al III blue and red troughs is 2:1. This means that the troughs are not saturated. We fit a single Gaussian to the Al III blue trough at 1854.72Å, and we used that Gaussian profile as the template for all other low-ionization troughs.

The Ly α and Ly β line troughs are highly saturated; the AOD column densities are 3200 and 9800 (in units of 10^{12} cm $^{-2}$), respectively. The different values indicate saturation, and we therefore use the higher value (Ly β 's) as a lower limit for the hydrogen column density.

The Mg II troughs are well separated but the red component's right wing is contaminated by the Mg II blue trough from another outflow system (see the feature at 8750Å [observed frame] in figure 2 top right panel). By adopting the Al III template fitting, we can factor out the contamination of this outflow system. The ratio between the blue and red components of Mg II is not exactly 2:1, which means they are mildly saturated. Therefore, for this situation we use the PC value.

C II, Al II, Si II and Si III are all singlets, thus the PC and PL models are not applicable and the saturation is undetermined. Therefore, we use the AOD method to get lower limits on their column densities.

3.4. The high-ionization troughs

In the Si IV doublet, we see several different outflow systems spanning $-3000 < v < -1500$ km s $^{-1}$. The deepest absorption trough at $-2200 < v < -1500$ km s $^{-1}$ is the one coinciding with the low-ionization and the S IV troughs. Although the multiple components blend with each other to some extent, one Gaussian profile can fit the blue and red components of Si IV between $-2200 < v < -1500$ km s $^{-1}$ quite well. The lower velocity wings are uncontaminated and well fitted by the Gaussian template. In Arav et al. (2018), it has been shown that the Si IV absorption trough itself can work as a good template for S IV troughs (see their figure 4). Here, we use the Gaussian profile fitted on the Si IV trough (1402.77Å) as the template for P V and S IV/S IV*, as they are blended with the Ly α forest (see figure 3 for more details).

The troughs from the P V doublet are important diagnostics in AGN outflows since the low abundance of phosphorous ($\sim 10^{-3}$ that of carbon in solar abundance; Lodders et al. 2009) makes the P V trough less likely to be saturated. Here, the blue wing of P V (1117.98Å) is clearly contaminated by Ly α forest absorption lines. However, the template fits the red wing of this trough quite well, thus allowing us to measure its full column density. In figure 3, the template fitting shows that the red and blue components of P V have a 1:2 optical depth ratio. Therefore, they are not saturated and the AOD measurement yields reliable column densities.

The high-ionization troughs C IV, N V and O VI, are highly saturated. We adopt their AOD results as the lower limits for their column densities.

4. PHOTOIONIZATION ANALYSIS

Photoionization is the dominant ionization mechanism in AGN outflows (Borguet et al. 2012a, 2013; Chamberlain & Arav 2015). We solve the ionization and thermal balance equations with the spectral synthesis code Cloudy (version c17.00), which is designed to simulate conditions in interstellar matter under a broad range of conditions (Ferland et al. 2017).

4.1. Photoionization Solution

We ran a grid of photoionization simulations using the spectral energy distribution, UV-soft SED (Dunn et al. 2010) and assumed solar metallicity. We varied the ionization parameter $\log(U_{\text{H}})$ between -5.0 and 3.0 in steps of 0.05 dex, with the stopping criterion that the ratio of the proton density to total hydrogen density ($\log(N_{\text{H}})$) equals 0.1. This stopping criterion ensures that the gas zones generated by Cloudy cover a large range of hydrogen column densities for each U_{H} , while optimizing the computation time when a region is near the hydrogen ionization front. Then we compared the predicted column densities from the grid model to our measurements for each ion. Each colored contour in figure 4 represents all possible solutions for the measured column density of a given ion. We then performed a χ^2 -minimization of the difference between the model and measured column densities to find the best-fit solution: $\log(N_{\text{H}}) = 21.47_{-0.27}^{+0.21}$ cm $^{-2}$ and $\log(U_{\text{H}}) = -1.23_{-0.25}^{+0.20}$. This solution is indicated by the red 'X' surrounded by the 1σ confidence level contour (see figure 4 for more details).

4.2. The Possibility of Multi-ionization Phases

Our photoionization analysis implicitly assumes that the outflowing material has one ionization phase. However, there are known cases of quasar outflows where at least two ionization components are needed (Arav et al. 2001; Gabel et al. 2005; Arav et al. 2013). Therefore, we need to address the ramification of such a possibility on our current analysis.

We start by noting that the photoionization solution we present in figure 4, fits the measured column density from all the troughs in our data. These troughs arise from low-ionization species such as Al II to the high-ionization P V. The good fit of a single ionization solution to all these measurements argues that we do not miss material with a lower ionization potential than P V.

However, there is the good possibility that a higher ionization phase exists and would have been revealed if we could observe troughs from higher ionization species (e.g., Ne VIII and Mg X Arav et al. 2013). Such a phase can contribute a larger N_{H} than the lower ionization phase (see Arav et al. 2013), increasing the derived mass flux and kinetic luminosity linearly with the total N_{H} (see equation 3). In contrast, the determination for the distance of the outflow from the central source (R) will probably not change appreciably (see section 6).

4.3. Dependency on SED and Metallicity

In order to show the influence the choice of SED and metallicity value have on the photoionization results, we consider different pairs of SEDs and metallicities following the approach of Arav et al. (2013) and Chamberlain et al. (2015). There are three different

SEDs used in Arav et al. (2013) along with two different metallicities for a total of six different cases. In figure 5, we present the results of each case, where the χ^2 -contours are shown in different colors. GASS10 (Grevesse et al. 2010) solar metallicity is used for Z1, and GASS10 with the scaling of Hamann & Ferland (1993) is used for four times solar metallicity (Z4). An increase in metallicity lowers the N_{H} value by roughly the same amount. This happens because the metals' column densities are fixed, and when the metallicity is increased, the column density ratios between the metals and hydrogen will increase. Therefore, the total hydrogen column density drops. The different SEDs and metallicities spread the solution over 0.3 and 1 dex for U_{H} and N_{H} , respectively.

5. THE DENSITY-SENSITIVE TROUGHS: S IV AND S IV*

The S IV* energy level is populated by electrons collisionally excited from the ground state by free electrons. Therefore, the ratio between the column densities of S IV* and S IV can be used as a diagnostic for the electron number density, n_e . The temperature of the S IV zone predicted by the Cloudy simulation from our adopted photoionization solution is 20,000K. From Arav et al. (2018), we have:

$$n_e \simeq n_{cr} \left[\frac{2N(\text{S IV})}{N(\text{S IV}^*)} e^{-\Delta E/kT} - 1 \right]^{-1} \quad (1)$$

where $n_{cr} = 6.3 \times 10^4 \text{ cm}^{-3}$ is the critical density for the excited/ground states at $T=20,000\text{K}$, $N(\text{S IV})$ and $N(\text{S IV}^*)$ are the column densities for the ground and excited states of S IV, respectively, ΔE is the energy difference between the levels, T is the temperature in Kelvin, and k is the Boltzmann constant. In practice,

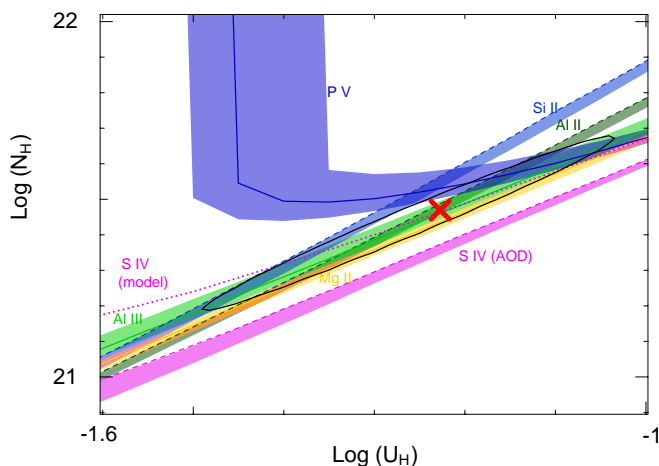


Figure 4. Grid-models showing the photoionization solution. For the studied outflow component in SDSS J1111+1437, we use the UV-soft SED (Dunn et al. 2010) and assume solar metallicity for the gas. Each colored contour represents the region of models (U_{H} , N_{H}) that predicts a column density consistent with the observed column density for that ion. Solid lines represent measurements, while dashed lines represent lower limits. The dotted line labeled “S IV (model)” is where we match the S IV column density to the photoionization solution (see section 5 for more details). The photoionization solution is the red ‘X’ and the 1σ error contour is the black ellipse. All other ion measurements in table 1 that are not shown here are lower limits below the plot range, but are consistent with the photoionization solution.

we compare our measured S IV*/S IV column density ratio to those predicted by a grid of collisional excitation models calculated from the CHIANTI 7.1.3 atomic database (Landi et al. 2013) to obtain the number density of the outflowing gas (see figure 6).

In order to obtain n_e from equation (1), we need reliable values for $N(\text{S IV})$ and $N(\text{S IV}^*)$. The AOD values for $N(\text{S IV})$ and $N(\text{S IV}^*)$ are given in table 1 and their combined value is plotted in figure 4, as the strip labeled “S IV (AOD)”. However, this “S IV (AOD)” contour does not intersect the photoionization solution. This is not surprising since $N(\text{S IV})$ and $N(\text{S IV}^*)$ are calculated using the AOD method and are therefore lower limits. To obtain the total $N(\text{S IV})$ that matches the solution, we ran a Cloudy model for the N_{H} and U_{H} values of the solu-

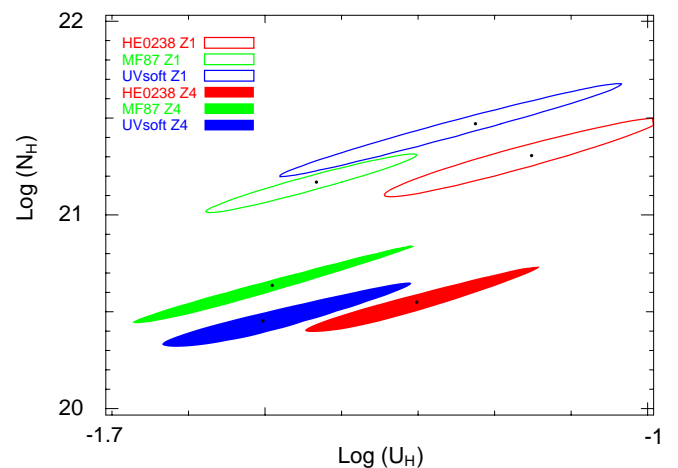


Figure 5. Grid-models showing the photoionization solution for three SEDs (HE0238, MF87 and UVsoft, see the descriptions in Arav et al. (2013)) and two metallicities: solar metallicity (Z1) and four times solar metallicity (Z4), for a total of six models.

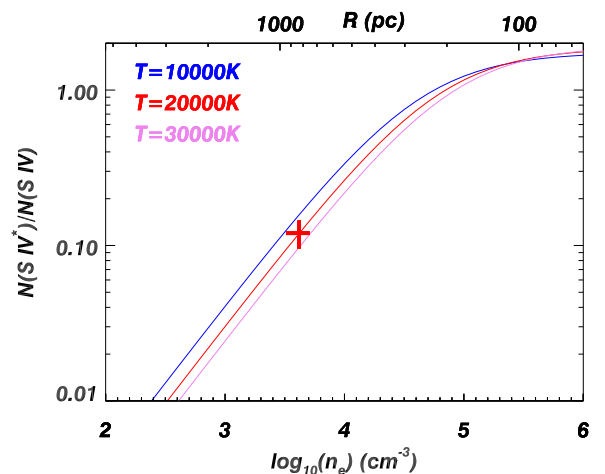


Figure 6. The S IV*/S IV column density ratio versus n_e from CHIANTI following Equation (1). The red cross matches the solution from the photoionization plot (see figure 4). To show the sensitivity of the derived n_e to temperature, we include the curves for three different temperatures. The mean temperature of the S IV gas in our Cloudy simulation from the photoionization solution is 20,000K. The top axis is the outflow’s distance from the central source using equation (2) (see section 6 for more details).

Table 2
Comparison with Other Energetic Quasar Outflows

Object	$\log(L_{Bol})$ erg s ⁻¹	BH Mass log(M/M _⊙)	v km s ⁻¹	$\log(U_H)$ log(cm ⁻²)	$\log(N_H)$ log(cm ⁻²)	$\log(n_e)$ log(cm ⁻³)	R pc	\dot{M} M _⊙ yr ⁻¹	Log \dot{E}_k log(erg s ⁻¹)	\dot{E}_k/L_{Edd}^d %
HE 0238-1904 ^a	47.2	-	-5000	-1.8 ⁺¹ _{-0.4}	20.7 ^{+0.09} _{-0.1}	4.5 ^{+0.2} _{-0.2}	1700 ⁺¹²⁰⁰ ₋₁₂₀₀	69 ⁺⁵⁰ ₋₅₀	45.4 ^{+0.3} _{-0.6}	1.6 ^{+1.3} _{-1.2} ⁽³⁾
J0318-0600 ^b	47.6	9.6	-4200	-3.1	19.9	3.3	6000	120	44.8	0.13
J0831+0354 ^c	46.9	8.8	-10,800	-0.3 ^{+0.5} _{-0.5}	22.5 ^{+0.5} _{-0.4}	4.4 ^{+0.3} _{-0.2}	110 ⁺³⁰ ₋₂₅	410 ⁺⁵³⁰ ₋₂₂₀	46.2 ^{+0.4} _{-0.3}	14 ⁺¹⁸ _{-7.7}
J0838+2955 ^b	47.5	9.0	-4900	-1.9 ^{+0.2} _{-0.2}	20.8 ^{+0.3} _{-0.3}	3.8 ^{+0.2} _{-0.2}	3300 ⁺¹⁵⁰⁰ ₋₁₀₀₀	300 ⁺²¹⁰⁰ ₋₁₂₀	45.4 ^{+0.2} _{-0.2}	2 ^{+1.2} _{-0.8}
J1106+1939 ^c	47.2	8.9	-8250	-0.5 ^{+0.3} _{-0.2}	22.1 ^{+0.3} _{-0.1}	4.1 ^{+0.02} _{-0.4}	320 ⁺²⁰⁰ ₋₁₀₀	390 ⁺³⁰⁰ ₋₁₀	46.0 ^{+0.3} _{-0.1}	12 ⁺¹¹ _{-0.3}
J1111+1437 ^c	46.9	9.2	-1860	-1.23 ^{+0.20} _{-0.25}	21.47 ^{+0.21} _{-0.27}	3.62 ^{+0.09} _{-0.11}	880 ⁺²¹⁰ ₋₂₆₀	55 ⁺¹⁰ ₋₁₁	43.8 ^{+0.07} _{-0.1}	0.03 ^{+0.005} _{-0.006}
J1206+1052 ^d	47.6	9.0	-1400	-1.82 ^{+0.12} _{-0.12}	20.46 ^{+0.2} _{-0.2}	3.03 ^{+0.06} _{-0.06}	840 ⁺⁶⁰ ₋₆₀	9 ⁺³ ₋₃	42.8 ^{+0.15} _{-0.15}	0.001 ^{+0.0005} _{-0.0025}

Note. —

(1). All solutions assumed the UV-soft SED with metallicity $Z = Z_{\odot}$, except for SDSS J0318-0600, the reddened UV-soft SED with $Z = 7.2Z_{\odot}$ is assumed; for SDSS J0838+2955, the modified MF87 SED with $Z = Z_{\odot}$ is assumed; and for SDSS J1106+1939, the UV-soft SED with $Z = 4Z_{\odot}$ is assumed.

(2). n_e is derived from:

^a high-ionization: O IV*/O IV.

^b low-ionization: Si II*/Si II.

^c high-ionization: S IV*/S IV.

^d S III*/S III and N III*/N III.

(3) For HE0238-1904, we report \dot{E}_k/L_{Bol} .

References: HE 0238-1904: Arav et al. (2013); SDSS J0318-0600: Dunn et al. (2010); SDSS J0831+0354: Chamberlain & Arav (2015); SDSS J0838+2955: Moe et al. (2009); SDSS J1106+1939: Borguet et al. (2013); SDSS J1111+1437: this work; SDSS J1206+1052: Chamberlain et al. (2015).

tion shown in figure 4. The predicted N(S IV) + N(S IV*) value is $N(S IV_{model-tot}) = 7140_{-950}^{+950} \times 10^{12} \text{ cm}^{-2}$, which we then plot as the “S IV (model)” contour in figure 4. Next, we need to obtain separate values for N(S IV) and N(S IV*). We can do so under the plausible assumption that the S IV and S IV* troughs share the same covering factor $C(v)$, and then use the partial-covering factor formalism (e.g., Dunn et al. 2010) to solve for both, which yields $N(S IV^*_{model}) = 860_{-130}^{+130} \times 10^{12} \text{ cm}^{-2}$. In this situation, the deeper S IV trough is much more saturated (around twice the AOD value) than the shallower S IV* trough (only 10% above its AOD value). We use these model values to recalculate the N(S IV*)/N(S IV) ratio (see figure 6), and obtain $\log(n_e) = 3.62_{-0.11}^{+0.09} \text{ cm}^{-3}$. Finally, in the high-ionization region where S IV is abundant, $n_e \simeq 1.2n_H$. Therefore, we derive a hydrogen number density of $\log(n_H) = 3.54_{-0.09}^{+0.08} \text{ cm}^{-3}$.

6. OUTFLOW DISTANCE AND ENERGETICS

A photoionized plasma is characterized by the ionization parameter U_H :

$$U_H = \frac{Q_H}{4\pi R^2 n_H c} \quad (2)$$

where $Q_H = 5.7 \times 10^{56} \text{ s}^{-1}$ is the source emission rate of hydrogen ionizing photons, R is the distance of the outflow to the central source, n_H is the number density of hydrogen, and c is the speed of light. We can obtain a measurement for R by solving equation (2), which yields the following result: the outflow of SDSS J1111+1437 is located at $R = 880_{-260}^{+210} \text{ pc}$ from the central source, where the errors come from adding in quadrature the errors for U_H and n_H .

We note that an additional higher ionization phase in the outflowing material would not affect the R determi-

nation appreciably. This is because such a higher ionization phase will have only a negligible amount of S IV. Therefore, the gas containing the S IV/S IV* we measure is almost entirely associated with the ionization solution we present in figure 4.

Assuming the outflow is in the form of a thin partial shell, its mass flow rate (\dot{M}) and kinetic luminosity (\dot{E}_k) are given by (Borguet et al. 2012a):

$$\dot{M} \simeq 4\pi\Omega RN_H \mu m_p v = 55_{-11}^{+10} M_{\odot} \text{ year}^{-1} \quad (3)$$

$$\dot{E}_k \simeq \frac{1}{2} \dot{M} v^2 = 6_{-1.2}^{+1.1} \times 10^{43} \text{ erg s}^{-1} \quad (4)$$

where R is the distance of the outflow from the central source, $\Omega = 0.08$ is the global covering factor for outflows showing S IV absorptions (Borguet et al. 2013), $\mu = 1.4$ is the mean atomic mass per proton, m_p is the proton mass, N_H is the absorber’s total hydrogen column density, and v is the radial velocity of the outflow. The results in equations (3) and (4) are calculated from the photoionization solution shown in figure 4, which uses the UV-soft SED and assumes solar metallicity (Dunn et al. 2010). As evident from the error ellipse in figure 4, N_H and U_H are correlated. Since R is a function of U_H , N_H and R are also correlated, and we took this into account in calculating the error quoted in equation (3).

6.1. Comparison with Other Objects

We compare our results with several other outflows which have distance and energetic determinations in the literature (see Table 2). As shown in the Introduction, \dot{E}_k values exceeding 0.5% (Hopkins & Elvis 2010) or 5% (Scannapieco & Oh 2004) of the Eddington luminosity are viewed to be potentially significant

for AGN feedback. For SDSS J1111+1437, the mass of the supermassive black hole (SMBH) is estimated to be $\log(M_{BH}/M_{\odot}) \sim 9.2$ [from the virial theorem and the full width half maximum (FWHM) of the CIV BEL using equation (3) of Park et al. (2013)]. The Eddington luminosity is then $L_{Edd} \sim 2 \times 10^{47} \text{ erg s}^{-1}$. Combined with the result from equation (4), our determination of $\dot{E}_k/L_{Edd} = 0.03\%$ shows that SDSS J1111+1437 does not have significant AGN feedback from this outflow. The other four higher-velocity outflows (see figure 1) might have higher \dot{E}_k . However, we lack the diagnostic troughs to measure their R and N_H .

7. SUMMARY

We presented an analysis of an outflow seen in quasar SDSS J1111+1437 based on observations from the VLT/X-shooter. Our results are summarized as follows:

1. We analyzed the outflow component that spans the velocity range -1500 to -2200 km s^{-1} with a velocity centroid of -1860 km s^{-1} in the quasar's rest-frame. This outflow component shows a variety of absorption troughs from both high and low-ionization species, for which we derive ionic column densities (see table 1).

2. From the density-sensitive troughs of SIV and SIV*, we determined the electron number density as $\log(n_e) = 3.62_{-0.11}^{+0.09} \text{ cm}^{-3}$. In the high-ionization region where SIV is abundant, $n_e \simeq 1.2n_H$, which gives a hydrogen number density of $\log(n_H) = 3.54_{-0.09}^{+0.08} \text{ cm}^{-3}$.

3. Using the derived column densities, we presented the photoionization plots in the $\log(N_H) - \log(U_H)$ phase space to find the photoionization solution. We also tested the dependency on the choice of SED and metallicity, and chose the UV-soft SED with solar metallicity as the representative result, which gave a column density for hydrogen of $\log(N_H) = 21.47_{-0.27}^{+0.21} \text{ cm}^{-2}$ and an ionization parameter of $\log(U_H) = -1.23_{-0.25}^{+0.20}$.

4. The distance of the outflow was determined to be $880_{-260}^{+210} \text{ pc}$ from the central source, along with a mass flow rate of $\dot{M} = 55_{-11}^{+10} M_{\odot} \text{ year}^{-1}$ and kinetic luminosity at 0.03% of the Eddington luminosity.

N.A. acknowledges support from NSF grant AST 1413319 as well as NASA STScI grants GO 11686, 12022, 14242, 14054, and 14176, and NASA ADAP 48020.

Based on observations collected at the European Organisation for Astronomical Research in the Southern Hemisphere under ESO programmes 092.B-0267 (PI: Benn).

REFERENCES

- Anglés-Alcázar, D., Davé, R., Faucher-Giguère, C.-A., Özel, F., & Hopkins, P. F. 2017, MNRAS, 464, 2840
Aoki, K., Oyabu, S., Dunn, J. P., et al. 2011, PASJ, 63, 457
Arav, N., Korista, K. T., de Kool, M., Junkkarinen, V. T., & Begelman, M. C. 1999, ApJ, 516, 27
Arav, N., de Kool, M., Korista, K. T., et al. 2001, ApJ, 561, 118
Arav, N., Moe, M., Costantini, E., et al. 2008, ApJ, 681, 954-964
Arav, N., Edmonds, D., Borguet, B., et al. 2012, A&A, 544, AA33
Arav, N., Borguet, B., Chamberlain, C., Edmonds, D., & Danforth, C. 2013, MNRAS, 436, 3286
Arav, N., Liu, G., Xu, X., et al. 2018, ApJ, 857, 60
Ballester, P., Bramich, D., Forchi, V., et al. 2011, Astronomical Data Analysis Software and Systems XX, 442, 261
Bautista, M. A., Dunn, J. P., Arav, N., et al. 2010, ApJ, 713, 25
Borguet, B. C. J., Edmonds, D., Arav, N., Dunn, J., & Kriss, G. A. 2012a, ApJ, 751, 107
Borguet, B. C. J., Edmonds, D., Arav, N., Benn, C., & Chamberlain, C. 2012, ApJ, 758, 69
Borguet, B. C. J., Arav, N., Edmonds, D., Chamberlain, C., & Benn, C. 2013, ApJ, 762, 49
Chamberlain, C., & Arav, N. 2015, MNRAS, 454, 675
Chamberlain, C., Arav, N., & Benn, C. 2015, MNRAS, 450, 1085
Choi, E., Naab, T., Ostriker, J. P., Johansson, P. H., & Moster, B. P. 2014, MNRAS, 442, 440
Ciotti, L., Ostriker, J. P., & Proga, D. 2010, ApJ, 717, 708
Ciotti, L., Pellegrini, S., Negri, A., & Ostriker, J. P. 2017, ApJ, 835, 15
de Kool, M., Arav, N., Becker, R. H., et al. 2001, ApJ, 548, 609
de Kool, M., Becker, R. H., Gregg, M. D., White, R. L., & Arav, N. 2002, ApJ, 567, 58
de Kool, M., Korista, K. T., & Arav, N. 2002, ApJ, 580, 54
Dai, X., Shankar, F., & Sivakoff, G. R. 2008, ApJ, 672, 108-114
Dunn, J. P., Crenshaw, D. M., Kraemer, S. B., & Trippe, M. L. 2010, ApJ, 713, 900
Dunn, J. P., Bautista, M., Arav, N., et al. 2010, ApJ, 709, 611
Dunn, J. P., Arav, N., Aoki, K., et al. 2012, ApJ, 750, 143
Edmonds, D., Borguet, B., Arav, N., et al. 2011, ApJ, 739, 7
Elvis, M. 2000, ApJ, 545, 63
Ferland, G. J., Porter, R. L., van Hoof, P. A. M., et al. 2013, ApJ, 49, 137
Ferland, G. J., Chatzikos, M., Guzmán, F., et al. 2017, RMxAA, 53, 385
Faucher-Giguère, C.-A., Quataert, E., & Murray, N. 2012, MNRAS, 420, 1347
Finn, C. W., Morris, S. L., Crighton, N. H. M., et al. 2014, MNRAS, 440, 3317
Gabel, J. R., Kraemer, S. B., Crenshaw, D. M., et al. 2005, ApJ, 631, 741
Gabel, J. R., Arav, N., & Kim, T.-S. 2006, ApJ, 646, 742
Ganguly, R., & Brotherton, M. S. 2008, ApJ, 672, 102-107
Grevesse, N., Asplund, M., Sauval, A. J., & Scott, P. 2010, Ap&SS, 328, 179
Hamann, F., & Ferland, G. 1993, ApJ, 418, 11
Hamann, F. W., Barlow, T. A., Chaffee, F. C., Foltz, C. B., & Weymann, R. J. 2001, ApJ, 550, 142
Hamann, F., & Sabra, B. 2004, AGN Physics with the Sloan Digital Sky Survey, 311, 203
Hewett, P. C., & Foltz, C. B. 2003, AJ, 125, 1784
Hopkins, P. F., & Elvis, M. 2010, MNRAS, 401, 7
Hopkins, P. F., Torrey, P., Faucher-Giguère, C.-A., Quataert, E., & Murray, N. 2016, MNRAS, 458, 816
Knigge, C., Scaringi, S., Goad, M. R., & Cottis, C. E. 2008, MNRAS, 386, 1426
Korista, K. T., Bautista, M. A., Arav, N., et al. 2008, ApJ, 688, 108-115
Landi, E., Young, P. R., Dere, K. P., Del Zanna, G., & Mason, H. E. 2013, ApJ, 763, 86
Lodders, K., Palme, H., & Gail, H.-P. 2009, Landolt Börnstein, Lucy, A. B., Leighly, K. M., Terndrup, D. M., Dietrich, M., & Gallagher, S. C. 2014, ApJ, 783, 58
McCarthy, I. G., Schaye, J., Ponman, T. J., et al. 2010, MNRAS, 406, 822
Moe, M., Arav, N., Bautista, M. A., & Korista, K. T. 2009, ApJ, 706, 525
Murray, N., Chiang, J., Grossman, S. A., & Voit, G. M. 1995, ApJ, 451, 498
Ostriker, J. P., Choi, E., Ciotti, L., Novak, G. S., & Proga, D. 2010, ApJ, 722, 642
Park, D., Woo, J.-H., Denney, K. D., & Shin, J. 2013, ApJ, 770, 87
Proga, D., Stone, J. M., & Kallman, T. R. 2000, ApJ, 543, 686
Savage, B. D., & Sembach, K. R. 1991, ApJ, 379, 245
Scannapieco, E., & Oh, S. P. 2004, ApJ, 608, 62
Soker, N., & Meiron, Y. 2011, MNRAS, 411, 1803
Sun, L., Zhou, H., Ji, T., et al. 2017, ApJ, 838, 88